Computation of Isolated Periodic Solutions for Forced Response Blade-Tip/Casing Contact Problems

Thibaut Vadcard, Fabrice Thouverez, Alain Batailly

POLYTECHNIQUE MONTRÉAL
UNIVERSITÉ D'INGÉNIERIE

LABORATOIRE D'ANALYSE VIBRATOIRE ET ACOUSTIQUE

Computation of isolated periodic solutions for forced response blade-tip/casing contact problems

T. Vadcard[1,2], F. Thouverez[2], A. Batailly[1]

Abstract

This article introduces a numerical procedure dedicated to the identification of isolated branches of solutions for nonlinear mechanical systems. It is here applied to a fan blade subject to rubbing interactions and harmonic forcing. Both contact, which is initiated by means of the harmonic forcing, and dry friction are accounted for. The presented procedure relies on the computation of the system's nonlinear normal modes and their analysis through the application of an energy principle derived from the Melnikov function. The dynamic Lagrangian frequency-time strategy associated with the harmonic balance method (DLFT-HBM) is used to predict the blade's dynamics response as well as to compute the autonomous nonlinear normal modes. The open industrial fan blade NASA rotor 67 is employed in order to avoid confidentiality issues and to promote the reproducibility of the presented results. Previous publications have underlined the complexity of NASA rotor 67's dynamics response as it undergoes structural contacts, thus making it an ideal benchmark blade when searching for isolated solutions. The application of the presented procedure considering a varying amplitude of the harmonic forcing allows to predict isolated branches of solutions featuring nonlinear resonances. With the use of the Melnikov energy principle, nonlinear modal interactions are shown to be responsible for the separation of branches of solutions from the main response curve. In the end, the application of the presented procedure on an industrial blade model with contact interactions demonstrates it is both industry-ready and applicable to highly nonlinear mechanical systems.

Keywords

Harmonic Balance Method, rotor/stator interaction, fan blade, nonlinear normal modes, isola, Melnikov energy principle

1 - Département de génie mécanique, École Polytechnique de Montréal, P.O. Box 6079, Succ. Centre-Ville, Montréal, Québec, Canada H3C 3A7
2 - École Centrale de Lyon, Laboratoire de Tribologie et Dynamique des Systèmes, UMR CNRS 5513, 36 avenue Guy de Collongue, Écully, 69134, France

Calcul de branches de solutions périodiques isolées pour des problèmes de contact aube/carter en réponse forcée

T. Vadcard[1,2], F. Thouverez[2], A. Batailly[1]

Résumé

Cet article présente une procédure numérique dédiée à l'identification de branches de solutions isolées pour les systèmes mécaniques non linéaires. Cette procédure est appliquée à une aube de soufflante soumise à des interactions de contact aube/carter et à un forçage harmonique. Le contact, qui est initié au moyen du forçage harmonique, et le frottement sec sont pris en compte. La procédure présentée repose sur le calcul des modes normaux non linéaires du système et leur analyse par l'application d'un principe d'énergie dérivé de la fonction de Melnikov. La stratégie *Dynamic Lagrangian Frequency-Time* associée à la méthode d'équilibrage harmonique (DLFT-HBM) est utilisée pour prédire la réponse dynamique de l'aube ainsi que pour calculer les modes normaux non linéaires. L'aube de soufflante industrielle NASA rotor 67 à géométrie ouverte est utilisée afin d'éviter les problèmes de confidentialité et de promouvoir la reproductibilité des résultats présentés. Des publications antérieures ont souligné la complexité de la réponse dynamique du NASA rotor 67 lorsqu'il subit des contacts structurels ce qui en fait une aube de référence idéale pour la recherche de solutions isolées. L'application de la procédure présentée avec une amplitude variable pour le forçage harmonique permet de prédire l'existence de branches de solutions isolées associées à des résonances non linéaires. L'utilisation du principe d'énergie de Melnikov permet de montrer que les interactions modales non linéaires sont impliquées dans la séparation des branches de solutions de la courbe de réponse principale. Enfin, l'application de la procédure présentée sur un modèle d'aube industrielle dans une configuration d'interaction de contact aube/carter démontre qu'elle est à la fois utilisable en conception industrielle et applicable à des systèmes mécaniques hautement non linéaires.

Mots-clés

Méthode d'équilibrage harmonique, rotor/stator interaction, aube de soufflante, modes normaux non linéaires, isolat, principe énergétique de Melnikov

1 - Département de génie mécanique, École Polytechnique de Montréal, P.O. Box 6079, Succ. Centre-Ville, Montréal, Québec, Canada H3C 3A7
2 - École Centrale de Lyon, Laboratoire de Tribologie et Dynamique des Systèmes, UMR CNRS 5513, 36 avenue Guy de Collongue, Écully, 69134, France

1 Introduction

In order to comply with international roadmaps for net carbon neutrality [1], aircraft engine manufacturers are committed to designing increasingly efficient turbomachines. To achieve this goal, the reduction of operating tip clearances is considered as a way to mitigate leakage flows and subsequent aerodynamic losses. However, this choice raises new challenges in the field of mechanical design as structural contacts between blades and their surrounding casing become more likely within nominal operating conditions [2, 3]. Therefore, accounting for these interactions in early design stages is now required. This calls for the development of efficient industry-ready predictive numerical strategies.

Strategies suitable for predictive simulations of rubbing interactions are of two types. (1) Those based on time marching simulations are the industrial state-of-the-art [4, 5, 6, 7]. However, such strategies face significant challenges for the prediction of periodic solutions, since reaching steady state can be computationally costly. This is the reason why (2) strategies in the frequency domain, specifically the harmonic balance method (HBM) [8, 9, 10, 11, 12], have known a renewed interest. Frequency domain strategies are also well-suited to provide a qualitative view of a system's dynamics including the stability analysis of predicted periodic solutions [13, 14, 15] and the connectivity of branches of solutions [9, 11, 16, 17].

Key features of numerical strategies dedicated to nonlinear dynamics simulations are inherently related to the type of investigated nonlinearity. Newly developed strategies are oftentimes applied to low-dimensional systems featuring smooth nonlinearities [17, 18, 19, 20, 21]. While such system may exhibit a very rich dynamics response, smooth nonlinearities do not present the same numerical challenges as those that may be found when dealing with nonsmooth nonlinearities such as contact. Because strategies developed for smooth nonlinearities rely on differentiability hypotheses, they may not apply to nonsmooth nonlinearities. Besides, even for smooth nonlinearities, industrial applications of predictive numerical strategies are scarce, thus justifying the development of numerical strategies dedicated to nonsmooth nonlinearities on large scale industrial systems.

Among the wide variety of nonlinear phenomena, the detection of isolated branches of solutions for mechanical systems is of particular interest. Indeed, isolated solutions have been identified as critical from a design viewpoint, notably due to the fact that they may feature higher amplitudes in frequency ranges beyond the predicted nonlinear resonances [16, 22, 23, 24]. Isolas—closed branches of solutions that are not connected to the main nonlinear frequency response curve of a system—have been predicted for many nonlinear applications [9, 16, 17, 18, 19, 21, 23, 25, 26, 27, 28]. Yet, no industrial standard strategy exist to systematically locate them accurately and efficiently. The use of homotopy [29], Gröbner bases [18, 30], limit-point bifurcation tracking [17] or the global terrain method [21] can lead to the identification of isolated solutions on low-dimensional systems, but these methodologies remain ill-suited for large scale non-regularized contact problems.

Recently, the analysis of nonlinear normal modes through the Melnikov energy principle was shown to accurately locate isolas on low-dimensional systems featuring both geometrical nonlinearities [19] and dry friction [26] at a low computational cost. Cenedese and Haller [19] provided mathematical justifications for the use of the energy balance method [31] that aims to predict nonlinear resonances in forced responses. The latter was recently extended to damped nonlinear normal modes [32, 33]. It allowed to locate isolated branches of solutions on a phenomenological model with friction contacts [33]. The study presented in this article demonstrates the applicability of the Melnikov energy principle on an industrial system featuring rubbing interactions, *i.e.* including both vibro-impact and dry friction. It provides an industry-ready numerical strategy for the prediction of high amplitude isolated branches of solutions. The second section presents all the methodological tools used in this paper including the HBM, the continuation procedure, the evaluation of nonlinear forces, the computation of complex nonlinear modes and the application of the Melnikov energy principle. The third section introduces the NASA rotor 67 model and the contact scenario. Finally, in the fourth section, results obtained by the application of the proposed isola detection procedure on the blade as well as an analysis focusing on the physical mechanisms favoring the apparition of isolated branches are presented in details.

2 Numerical isola detection procedure

2.1 Harmonic balance method

The time and space-normalized nonlinear equation of motion for a n-dof (degrees of freedom) mechanical system with respect to time reads

$$\frac{\alpha}{\beta^2}\mathbf{M}\ddot{\mathbf{x}}(t)+\frac{\alpha}{\beta}\mathbf{C}\dot{\mathbf{x}}(t)+\alpha\mathbf{K}\mathbf{x}(t)+\mathbf{f}_{\mathrm{nl}}(\mathbf{x}(t),\dot{\mathbf{x}}(t),\omega)=\mathbf{f}_{\mathrm{ex}}(\omega,t) \tag{1}$$

with $\mathbf{x}(t)$ the unknown displacement field, $\mathbf{M}$, $\mathbf{C}$ and $\mathbf{K}$ respectively the mass, damping and stiffness matrices of the system. $\mathbf{f}_{\mathrm{nl}}(\mathbf{x}(t),\dot{\mathbf{x}}(t),\omega)$ is the vector of nonlinear forces and $\mathbf{f}_{\mathrm{ex}}(\omega,t)$ the vector of monoharmonic excitation forces of pulsation ω. Overdots refer to derivatives with respect to time t. α and β are respectively space and time normalization coefficients, chosen so that $\|\alpha\mathbf{x}(t)\|\simeq 1$ and $\omega/\beta\simeq 1$.

The HBM relies on the assumption that $\mathbf{x}(t)$, $\mathbf{f}_{\mathrm{nl}}(\mathbf{x}(t),\dot{\mathbf{x}}(t),\omega)$ and $\mathbf{f}_{\mathrm{ex}}(\omega,t)$ can be written as a N_{h}-truncated Fourier series of fundamental pulsation ω, such as

$$\begin{cases}\mathbf{x}(t)\simeq\dfrac{1}{2}\mathbf{a}_0+\displaystyle\sum_{k=1}^{N_{\mathrm{h}}}\left(\mathbf{a}_k\cos(k\omega t)+\mathbf{b}_k\sin(k\omega t)\right) & \text{(2a)}\\ \mathbf{f}_{\mathrm{nl}}(t)\simeq\dfrac{1}{2}\mathbf{a}_0^{\mathrm{nl}}+\displaystyle\sum_{k=1}^{N_{\mathrm{h}}}\left(\mathbf{a}_k^{\mathrm{nl}}\cos(k\omega t)+\mathbf{b}_k^{\mathrm{nl}}\sin(k\omega t)\right) & \text{(2b)}\\ \mathbf{f}_{\mathrm{ex}}(t)\simeq\dfrac{1}{2}\mathbf{a}_0^{\mathrm{ex}}+\displaystyle\sum_{k=1}^{N_{\mathrm{h}}}\left(\mathbf{a}_k^{\mathrm{ex}}\cos(k\omega t)+\mathbf{b}_k^{\mathrm{ex}}\sin(k\omega t)\right) & \text{(2c)}\end{cases}$$

where $\mathbf{a}_k^\bullet$ and $\mathbf{b}_k^\bullet$ with $\bullet\in\{-,\mathrm{nl},\mathrm{ex}\}$ are the real coefficients of the Fourier decompositions of each variable. By carrying out a Fourier-Galerkin procedure on the equation of motion, the differential nonlinear equation of motion Eqs. (1) becomes the nonlinear algebraic equation

$$\mathcal{H}(\widetilde{\mathbf{x}},\omega)=\mathbf{Z}(\omega)\widetilde{\mathbf{x}}+\widetilde{\mathbf{f}}_{\mathrm{nl}}(\widetilde{\mathbf{x}})-\widetilde{\mathbf{f}}_{\mathrm{ex}}=\mathbf{0}. \tag{3}$$

All Fourier coefficients are gathered in so-called multiharmonic vectors of size $n(2N_{\mathrm{h}}+1)$, such as

$$\begin{cases}\widetilde{\mathbf{x}}=[\frac{1}{2}\mathbf{a}_0^\top\ \mathbf{a}_1^\top\ \mathbf{b}_1^\top\ \dots\ \mathbf{a}_{N_{\mathrm{h}}}^\top\ \mathbf{b}_{N_{\mathrm{h}}}^\top]^\top & \text{(4a)}\\ \widetilde{\mathbf{f}}_{\mathrm{nl}}=[\frac{1}{2}(\mathbf{a}_0^{\mathrm{nl}})^\top\ (\mathbf{a}_1^{\mathrm{nl}})^\top\ (\mathbf{b}_1^{\mathrm{nl}})^\top\ \dots\ (\mathbf{a}_{N_{\mathrm{h}}}^{\mathrm{nl}})^\top\ (\mathbf{b}_{N_{\mathrm{h}}}^{\mathrm{nl}})^\top]^\top & \text{(4b)}\\ \widetilde{\mathbf{f}}_{\mathrm{ex}}=[\frac{1}{2}(\mathbf{a}_0^{\mathrm{ex}})^\top\ (\mathbf{a}_1^{\mathrm{ex}})^\top\ (\mathbf{b}_1^{\mathrm{ex}})^\top\ \dots\ (\mathbf{a}_{N_{\mathrm{h}}}^{\mathrm{ex}})^\top\ (\mathbf{b}_{N_{\mathrm{h}}}^{\mathrm{ex}})^\top]^\top. & \text{(4c)}\end{cases}$$

The multiharmonic vector $\widetilde{\mathbf{x}}$ is the new unknown vector of the problem.The dynamic stiffness matrix $\mathbf{Z}(\omega)$ contains the linear part of the problem and is block-diagonal with its $N_{\mathrm{h}}+1$ blocks $\mathbf{Z}_0$ and $\mathbf{Z}_k$ for $k\in[\![1,N_{\mathrm{h}}]\!]$ being

$$\mathbf{Z}_0=\alpha\mathbf{K}\text{ and }\mathbf{Z}_k(\omega)=\alpha\begin{bmatrix}\mathbf{K}-\left(\dfrac{k\omega}{\beta}\right)^2\mathbf{M} & \dfrac{k\omega}{\beta}\mathbf{C}\\ -\dfrac{k\omega}{\beta}\mathbf{C} & \mathbf{K}-\left(\dfrac{k\omega}{\beta}\right)^2\mathbf{M}\end{bmatrix}. \tag{5}$$

For the sake of computational efficiency, the size of the HBM equation Eqs. (3) is reduced by using an exact condensation procedure of the linear dof [34]. The final size of the system becomes $n_{\mathrm{nl}}(2N_{\mathrm{h}}+1)$ where n_{nl} is the number of nonlinear dof. The resulting quantities are subscripted $\bullet_{\mathrm{r}}$ and the condensed algebraic equation of motion reads

$$\mathcal{H}_{\mathrm{r}}(\widetilde{\mathbf{x}}_{\mathrm{r}},\omega)=\mathbf{Z}_{\mathrm{r}}(\omega)\widetilde{\mathbf{x}}_{\mathrm{r}}+\widetilde{\mathbf{f}}_{\mathrm{nl,r}}-\widetilde{\mathbf{f}}_{\mathrm{ex,r}}=\mathbf{0}. \tag{6}$$

2.2 Path following

2.2.1 Arc-length continuation

For highly nonlinear applications such as contact, nonlinear frequency response curves (NFRC) feature complex behaviors such as turning points thus yielding multiple solutions for given values of the control parameter ω. To go through the NFRC, a path following technique must be employed. The arc-length continuation [35] is used in this study. It is based on a prediction-correction scheme. The correction phase is carried out by a Newton-Raphson solver according to the so-called arc-length parameterization of the curve. The control parameter ω is considered as an unknown of the problem, thus increasing the dimension of the problem to solve. The augmented unknown vector is noted $\mathbf{y} = \left[\widetilde{\mathbf{x}}_{\mathrm{r}}^{\top}, \omega\right]^{\top}$.

Prediction The arc-length path following technique is based on a Newton-Raphson root-finding technique. A secant prediction is used to obtain an initial guess of the solution. This estimate $\mathbf{y}_{i+1}^{0}$ for the $(i+1)$-th point is computed by using the last two solutions $\mathbf{y}_i$ and $\mathbf{y}_{i-1}$, so that

$$\mathbf{y}_{i+1}^{0} = \mathbf{y}_i + \Delta s_i \frac{\Delta \mathbf{y}_i}{\|\Delta \mathbf{y}_i\|_2} \tag{7}$$

where $\Delta \mathbf{y}_i = \mathbf{y}_i - \mathbf{y}_{i-1}$ and Δs_i is the size of the prediction step at the i-th iteration.

Parameterization A parameterization equation $\mathcal{P}_\omega(\mathbf{y})$ must be added to solve the augmented problem. The solution at iteration $(i+1)$ is searched on an hypersphere of radius Δs_i centered around $\mathbf{y}_i$ in the $(n_{\mathrm{nl}}(2N_{\mathrm{h}}+1)+1)$-dimensional resolution space. It is done by ensuring the respect of

$$\mathcal{P}_\omega(\mathbf{y}) = \|\widetilde{\mathbf{x}}_{\mathrm{r}} - \widetilde{\mathbf{x}}_{\mathrm{r},i}\|_2^2 + (\omega - \omega_i)^2 - \Delta s_i^2 = 0. \tag{8}$$

Correction The correction step is carried out with an iterative Newton-Raphson root-finding technique solving for $\mathbf{y}$ the equation $\mathcal{G}(\mathbf{y}) = \left[\mathcal{H}_{\mathrm{r}}{}^{\top}(\mathbf{y}), \mathcal{P}_\omega(\mathbf{y})\right]^{\top} = \mathbf{0}$, including both the equation of motion Eqs. (6) and the parameterization equation Eqs. (8). The solution is found by successively correcting the estimate of the solution, such as at the $(k+1)$-th correction $\Delta \mathbf{y}^{k+1}$ is computed following $\dfrac{\partial \mathcal{G}}{\partial \mathbf{y}}(\mathbf{y}^k)\Delta \mathbf{y}^{k+1} = -\mathcal{G}(\mathbf{y}^k)$ with the next iterate being $\mathbf{y}^{k+1} = \mathbf{y}^k + \Delta \mathbf{y}^{k+1}$. A solution is found when the residual function is sufficiently close to zero, ensured by a user-defined tolerance δ, such that a solution is considered to be converged when $\|\mathcal{G}(\mathbf{y})\|_2^2 < \delta$. The arc-length procedure is illustrated in Fig. 1a.

2.2.2 Closed loop control

Isolated branches of solutions are encountered in this study, justifying the need of a closed loop detection procedure. Since these branches are isolated, the continuation must stop when it has looped over the whole branch. For this purpose, a geometric condition is used in this article.

At the beginning of the continuation procedure, the first point $\mathbf{y}_0 = \left[\widetilde{\mathbf{x}}_{\mathrm{r},0}^{\top}, \omega_0\right]^{\top}$ is saved as a reference point. Then, if two successive points cross the reference value ω_0 of the control parameter such as $\omega_i < \omega_0 < \omega_{i+1}$ or $\omega_{i+1} < \omega_0 < \omega_i$, then a closed loop test is carried out. An estimation of the solution $\widetilde{\mathbf{x}}_{\mathrm{r,int}}$ at $\omega = \omega_0$ is interpolated between ω_i and ω_{i+1} by means of

$$\widetilde{\mathbf{x}}_{\mathrm{r,int}} = \widetilde{\mathbf{x}}_{\mathrm{r},i} + \frac{\omega_0 - \omega_i}{\omega_{i+1} - \omega_i}(\widetilde{\mathbf{x}}_{\mathrm{r},i+1} - \widetilde{\mathbf{x}}_{\mathrm{r},i}). \tag{9}$$

If the relative distance d_{int} between $\widetilde{\mathbf{x}}_{\mathrm{r,int}}$ and $\widetilde{\mathbf{x}}_{\mathrm{r},0}$, computed by the formula

$$d_{\mathrm{int}} = \frac{\|\widetilde{\mathbf{x}}_{\mathrm{r,int}} - \widetilde{\mathbf{x}}_{\mathrm{r},0}\|_2}{\|\widetilde{\mathbf{x}}_{\mathrm{r,int}}\|_2}, \tag{10}$$

is lower than the user-defined tolerance d_{tol}, an isolated branch of solutions is detected and the continuation stops. The closed loop test is illustrated in Fig. 1b.

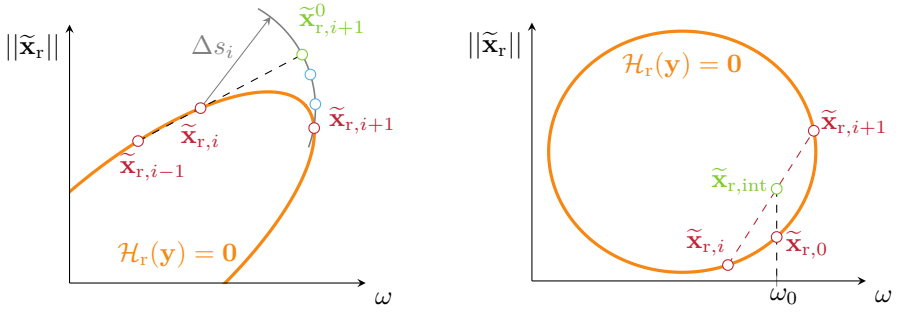

(a) arc-length continuation **(b)** closed loop control

Figure 1. Continuation strategy, solutions subspace (—), direction of research (—), solutions (○), prediction (○), correction iterations (○).

2.3 Dynamic Lagrangian frequency-time

The dynamic Lagrangian frequency-time procedure [8] is used to compute the nonlinear forces associated with contact interactions. This strategy is an extension of the alternating frequency-time (AFT) methodology [36]. It has been widely used to predict the dynamics of blade/disk assemblies [21, 28, 37, 38]. The DLFT-HBM was also recently shown to be well-suited for stiff vibro-impact contexts [16, 34].

2.3.1 Fourier matrices

The IDFT consists in reconstructing a time-discrete signal on N_t evenly spaced instants from the knowledge of the coefficients of its N_h-truncated Fourier series and using the associated Fourier basis $\mathbf{B}_{N_\mathrm{h}}(t)$ that read

$$\mathbf{B}_{N_\mathrm{h}}(t) = \left[\frac{1}{2}, \cos(\omega t), \sin(\omega t), \ldots, \cos(N_\mathrm{h}\omega t), \sin(N_\mathrm{h}\omega t)\right]^\top. \tag{11}$$

The IDFT is carried out by means of a matrix multiplication of the multiharmonic vector $\widetilde{\mathbf{z}}$. For a given time-dependent scalar variable $z(t)$, an IDFT corresponds to the computation of $\mathbf{z}$ such as

$$\mathbf{z} = [z(t_1), z(t_2), \ldots, z(t_{N_\mathrm{t}-1}), z(t_{N_\mathrm{t}})]^\top = \overline{\mathcal{F}}_1 \widetilde{\mathbf{z}} \tag{12}$$

with the IDFT matrix $\overline{\mathcal{F}}_1$ being

$$\overline{\mathcal{F}}_1 = \left[[\mathbf{B}_{N_\mathrm{h}}(t_1)| \ldots |\mathbf{B}_{N_\mathrm{h}}(t_i)| \ldots |\mathbf{B}_{N_\mathrm{h}}(t_{N_\mathrm{t}})]^\top\right]. \tag{13}$$

The DFT matrix is defined as the Moore-Penrose pseudo-inverse of $\overline{\mathcal{F}}_1$, *i.e.* so that $\overline{\mathcal{F}}_1 \mathcal{F}_1 = \mathbf{I}_{N_\mathrm{t}}$, and it reads

$$\mathcal{F}_1 = \overline{\mathcal{F}}_1^\top \left(\overline{\mathcal{F}}_1 . \overline{\mathcal{F}}_1^\top\right)^{-1}. \tag{14}$$

The DFT and IDFT matrices can be extended to the transformation of vectorial variables of size n by Kronecker products, such as

$$\mathcal{F}_n = \mathcal{F}_1 \otimes \mathbf{I}_n \quad \text{and} \quad \overline{\mathcal{F}}_n = \overline{\mathcal{F}}_1 \otimes \mathbf{I}_n. \tag{15}$$

2.3.2 Evaluation of nonlinear forces

The computation of the nonlinear forces with DLFT-HBM is based on a prediction-correction algorithm. The underlying mathematical formalism relies on augmented Lagrangians [39]: unilateral contact constraints are ensured by the introduction of a penalization term including a supplementary unknown displacement field $\widetilde{\mathbf{y}}_\mathrm{r}$. The purpose

and properties of $\widetilde{\mathbf{y}}_\mathrm{r}$ are addressed further in the section. The normal contact forces associated with the augmented Lagrangian formalism leads to

$$\widetilde{\mathbf{f}}^\mathrm{N}_{\mathrm{nl,r}} = \widetilde{\mathbf{f}}_{\mathrm{ex,r}} - \mathbf{Z}_\mathrm{r}(\omega)\widetilde{\mathbf{x}}_\mathrm{r} - \varepsilon(\widetilde{\mathbf{g}}_{\mathbf{x},\mathrm{r}} - \widetilde{\mathbf{g}}_{\mathbf{y},\mathrm{r}}) \tag{16}$$

where $\widetilde{\mathbf{g}}_{\mathbf{x},\mathrm{r}}$ and $\widetilde{\mathbf{g}}_{\mathbf{y},\mathrm{r}}$ are multiharmonic vectors representing the gap functions respectively associated with $\widetilde{\mathbf{x}}_\mathrm{r}$ and $\widetilde{\mathbf{y}}_\mathrm{r}$ such as $\widetilde{\mathbf{g}}_{\mathbf{x},\mathrm{r}} = \mathcal{F}_{n_\mathrm{nl}}\mathbf{d} - \widetilde{\mathbf{x}}_\mathrm{r}$ and $\widetilde{\mathbf{g}}_{\mathbf{y},\mathrm{r}} = \mathcal{F}_{n_\mathrm{nl}}\mathbf{d} - \widetilde{\mathbf{y}}_\mathrm{r}$ with $\mathbf{d} = \{d(t_i)\}_{i=1\dots N_\mathrm{t}}$ vector containing the distance between the undeformed structure and the obstacle on each nonlinear node at each instant. ε is a weighting coefficient and $\widetilde{\mathbf{x}}_\mathrm{r}$ is the estimate of the solution displacement field at the current iteration of the Newton-Raphson procedure. The DLFT-HBM procedure relies on the fact that $\widetilde{\mathbf{y}}_\mathrm{r}$ is strictly admissible in terms of contact conditions, so that at convergence, *i.e.* when $\widetilde{\mathbf{x}}_\mathrm{r}$ is also admissible in terms of contact conditions, the term $\varepsilon(\widetilde{\mathbf{g}}_{\mathbf{x},\mathrm{r}} - \widetilde{\mathbf{g}}_{\mathbf{y},\mathrm{r}})$ vanishes. This hypothesis is satisfied by the way the contact constraints are handled in DLFT-HBM. Indeed, the term $\widetilde{\mathbf{y}}_\mathrm{r}$ is computed in a manner so that all unilateral contact conditions are enforced in the time domain.

The computation of the contact forces is carried out by a prediction-correction scheme. The contact forces of (16) are decomposed such as $\widetilde{\mathbf{f}}^\mathrm{N}_{\mathrm{nl,r}} = \widetilde{\mathbf{f}}^\mathrm{N}_{\mathrm{nl,pre}} + \widetilde{\mathbf{f}}^\mathrm{N}_{\mathrm{nl,cor}}$ where $\widetilde{\mathbf{f}}^\mathrm{N}_{\mathrm{nl,pre}} = \widetilde{\mathbf{f}}_{\mathrm{ex,r}} - \mathbf{Z}_\mathrm{r}(\omega)\widetilde{\mathbf{x}}_\mathrm{r} - \varepsilon\widetilde{\mathbf{g}}_{\mathbf{x},\mathrm{r}}$ and $\widetilde{\mathbf{f}}^\mathrm{N}_{\mathrm{nl,cor}} = \varepsilon\widetilde{\mathbf{g}}_{\mathbf{y},\mathrm{r}}$. Following the hypothesis that $\widetilde{\mathbf{y}}_\mathrm{r}$ is admissible in terms of unilateral contact conditions, the corrections should be computed in the time domain so that they ensure

$$\mathbf{0} \leq \mathbf{f}^\mathrm{N}_{\mathrm{nl,r}} \perp \mathbf{g}_{\mathbf{y},\mathrm{r}} \geq \mathbf{0}. \tag{17}$$

In order to correct the nonlinear forces as stated, it is necessary to transform $\widetilde{\mathbf{f}}^\mathrm{N}_{\mathrm{nl,pre}}$ into the time domain, such as $\mathbf{f}^\mathrm{N}_{\mathrm{nl,pre}} = \overline{\mathcal{F}}_{n_\mathrm{nl}}\widetilde{\mathbf{f}}^\mathrm{N}_{\mathrm{nl,pre}}$. The state of contact is predicted thanks to the sign of the prediction $\mathbf{f}^\mathrm{N}_{\mathrm{nl,pre}}(t_i)$ at every time t_i. The state of contact is then used to decide whether $\mathbf{g}_{\mathbf{y},\mathrm{r}}(t_i)$ should be zero or not, determining in the mean time the value of the correction since $\widetilde{\mathbf{f}}^\mathrm{N}_{\mathrm{nl,cor}} = \varepsilon\widetilde{\mathbf{g}}_{\mathbf{y},\mathrm{r}}$:

- **contact** ($\mathbf{f}^\mathrm{N}_{\mathrm{nl,pre}}(t_i) > 0$): $\mathbf{g}_{\mathbf{y},\mathrm{r}}(t_i) = 0$ implying that $\mathbf{f}^\mathrm{N}_{\mathrm{nl,cor}}(t_i) = 0$,
- **separation** ($\mathbf{f}^\mathrm{N}_{\mathrm{nl,pre}}(t_i) \leq 0$): $\mathbf{g}_{\mathbf{y},\mathrm{r}}(t_i) \neq 0$ implying that $\mathbf{f}^\mathrm{N}_{\mathrm{nl,r}}(t_i) = 0$, thus $\mathbf{f}^\mathrm{N}_{\mathrm{nl,cor}}(t_i) = -\mathbf{f}^\mathrm{N}_{\mathrm{nl,pre}}(t_i)$.

At this point, the value of $\widetilde{\mathbf{y}}_\mathrm{r}$ is fully known because it is expressed as a function of $\widetilde{\mathbf{g}}_{\mathbf{y},\mathrm{r}}$. After this phase of correction, the contact forces are transformed back to the frequency domain where they are used to evaluate the residual function $\mathcal{H}_\mathrm{r}(\widetilde{\mathbf{x}}_\mathrm{r}, \omega)$ following

$$\mathcal{H}_\mathrm{r}(\widetilde{\mathbf{x}}_\mathrm{r}, \omega) = \mathbf{Z}_\mathrm{r}(\omega)\widetilde{\mathbf{x}}_\mathrm{r} - \widetilde{\mathbf{f}}_{\mathrm{ex,r}} + \underbrace{\widetilde{\mathbf{f}}_{\mathrm{ex,r}} - \mathbf{Z}_\mathrm{r}(\omega)\widetilde{\mathbf{x}}_\mathrm{r} - \varepsilon(\widetilde{\mathbf{g}}_{\mathbf{x},\mathrm{r}} - \widetilde{\mathbf{g}}_{\mathbf{y},\mathrm{r}})}_{\widetilde{\mathbf{f}}^\mathrm{N}_{\mathrm{nl,r}}} = \mathbf{0}, \tag{18}$$

which finally yields

$$\mathcal{H}_\mathrm{r}(\widetilde{\mathbf{x}}_\mathrm{r}, \omega) = -\varepsilon(\widetilde{\mathbf{g}}_{\mathbf{x},\mathrm{r}} - \widetilde{\mathbf{g}}_{\mathbf{y},\mathrm{r}}) = \mathbf{0}. \tag{19}$$

Once the residual function Eqs. (18) has reached zero, $\widetilde{\mathbf{g}}_{\mathbf{x},\mathrm{r}} = \widetilde{\mathbf{g}}_{\mathbf{y},\mathrm{r}}$ so $\widetilde{\mathbf{x}}_\mathrm{r}$ is admissible in terms of unilateral contact conditions. The equation of equilibrium is then also verified because (16) ensures that $\widetilde{\mathbf{x}}_\mathrm{r}$ is a solution of the equation of motion when $\varepsilon(\widetilde{\mathbf{g}}_{\mathbf{x},\mathrm{r}} - \widetilde{\mathbf{g}}_{\mathbf{y},\mathrm{r}}) = \mathbf{0}$. The whole contact problem is then solved. The prediction-correction procedure is summed up in Fig. 2. In order to guarantee the convergence of the strategy in the iterative solver, the jacobian matrix $\mathcal{J} = \frac{\partial \mathcal{H}_\mathrm{r}}{\partial \widetilde{\mathbf{x}}_\mathrm{r}}(\widetilde{\mathbf{x}}_\mathrm{r}, \omega)$ is evaluated through an analytical procedure [34, 40].

2.4 Complex nonlinear normal modes

In a nonlinear framework, the modal properties (eigenfrequencies and mode shapes) of a system are dependent on the energy of the response. For that reason, linear modal analysis may only be considered in a nonlinear context for low amplitudes or weakly nonlinear phenomena. In the literature, several mathematical formalisms have been introduced [41, 42, 43, 44] to go beyond this roadblock which led to various definitions of nonlinear normal modes (NNM). In this article, the notion of complex nonlinear mode [44] is retained as it is well-suited in a HBM framework: it is based on the resolution of the nonconservative autonomous equation of motion

$$\frac{\alpha}{\beta^2}\mathbf{M}\ddot{\mathbf{x}}(t) + \frac{\alpha}{\beta}\mathbf{C}\dot{\mathbf{x}}(t) + \alpha\mathbf{K}\mathbf{x}(t) + \mathbf{f}_\mathrm{nl}(\mathbf{x}(t), \dot{\mathbf{x}}(t)) = \mathbf{0} \tag{20}$$

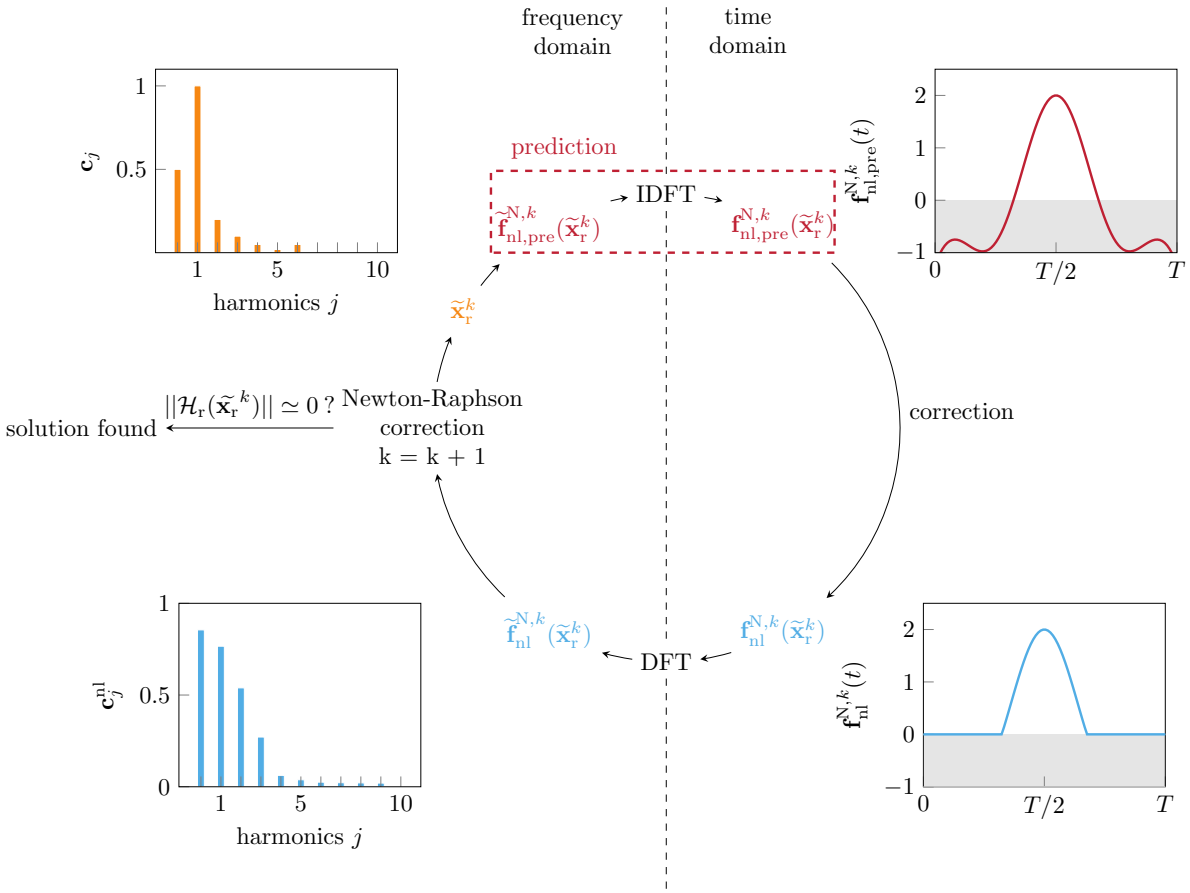

Figure 2. DLFT-HBM procedure, $c_j^\bullet = \sqrt{(a_j^\bullet)^2 + (b_j^\bullet)^2}$.

In order to account for the nonconservative nature of the equation, the shape of the solution $\mathbf{x}(t)$ is assumed to be an exponentially decaying N_h-truncated Fourier series, such as

$$\mathbf{x}(t) \simeq \frac{\mathbf{a}_0}{2} + \sum_{k=1}^{N_\mathrm{h}} e^{-k\zeta t} \left(\mathbf{a}_k \cos(k\omega t) + \mathbf{b}_k \sin(k\omega t) \right). \tag{21}$$

Under the hypothesis that the decaying factor ζ is small compared to ω, *i.e.* $\zeta \ll \omega$, the DLFT-HBM can be employed to solve (20). It only requires a modification of the dynamic stiffness matrix $\mathbf{Z}(\omega)$. Its blocks $\mathbf{Z}_k$ for $k \in [\![1, N_\mathrm{h}]\!]$ become

$$\mathbf{Z}_k = \alpha \begin{bmatrix} \mathbf{A} & -\mathbf{B} \\ \mathbf{B} & \mathbf{A} \end{bmatrix} \tag{22}$$

with

$$\mathbf{A} = \mathbf{K} - \frac{k\zeta}{\beta}\mathbf{C} - \frac{k^2\omega^2 - k^2\zeta^2}{\beta^2}\mathbf{M} \tag{23}$$

and

$$\mathbf{B} = \frac{2k^2\omega\zeta}{\beta^2}\mathbf{M} - \frac{k\omega}{\beta}\mathbf{C}. \tag{24}$$

NNM are computed with an arc-length continuation procedure. Since ζ is a new unknown of the problem, the arc-length parameterization equation should be changed to

$$\mathcal{P}_\omega(\widetilde{\mathbf{x}}_\mathrm{r}, \omega, \zeta) = \|\widetilde{\mathbf{x}}_\mathrm{r} - \widetilde{\mathbf{x}}_{\mathrm{r},i-1}\|^2 + (\omega - \omega_{i-1})^2 + (\zeta - \zeta_{i-1})^2 - \Delta s_i^2 = 0. \tag{25}$$

An additional equation is needed in order to close the augmented system of dimension $(n_\mathrm{nl}(2N_\mathrm{h}+1)+2)$. In this work, a phase condition on the displacement of a control dof is imposed by

$$\mathcal{P}_\zeta(\widetilde{\mathbf{x}}_\mathrm{r}) = \langle \mathbf{b}_\mathrm{contr}, (\mathbf{B}_{N_\mathrm{h}}(t_1))^\top \widetilde{\mathbf{x}}_\mathrm{r} \rangle = \mathbf{x}_\mathrm{contr}(t_1) = 0 \tag{26}$$

where $\mathbf{b}_\mathrm{contr}$ is a boolean vector composed of zeros but on the control dof where it contains a one, restraining the phase condition to the control dof. Equation Eqs. (26) ensures that the displacement of the control dof $\mathbf{x}_\mathrm{contr}$ is null when $t = t_1 = 0$. In practice, the continuation of a NNM is initialized at a low amplitude in the linear domain where the NNM is coincident with the linear free vibration mode.

2.5 Melnikov energy principle for nonconservative systems

The analysis of conservative autonomous solutions through the Melnikov energy principle, proposed by Cenedese and Haller [19], was recently shown to accurately predict the existence of isolated branches of solutions on low-dimensional models featuring geometrical nonlinearities [19] and dry friction [26]. From the knowledge of a conservative autonomous solutions family, the Melnikov energy principle allows to state if these solutions persist when adding a nonconservative perturbation $\mathcal{Q}$ of the form

$$\mathcal{Q}(\mathbf{x}, \dot{\mathbf{x}}, \tau) = A\mathbf{f}_\mathrm{ex}\cos(\omega\tau) - \mathbf{C}\dot{\mathbf{x}} - \mathbf{f}_\mathrm{nl}(\mathbf{x}, \dot{\mathbf{x}}, \omega) \tag{27}$$

to the conservative equation of motion, where $\mathbf{f}_\mathrm{ex}$ is a normalized excitation shape and A a dimensionless amplitude. The Melnikov energy principle relies on the analysis of the estimated work of the perturbation $\mathcal{Q}$ associated with a conservative NNM trajectory $\mathbf{x}_\mathrm{c}(t)$. In this paper, the case of a perturbation $\mathcal{Q}$ with the same periodicity as the autonomous solutions $\mathbf{x}_\mathrm{c}(t)$ is investigated, noted by the $\bullet^{1:1}$ superscript. The work of the perturbation can be written as the so-called Melnikov function

$$\mathcal{M}^{1:1} = w^{1:1}(A, \mathbf{f}_\mathrm{ex}, t) - \mathcal{R}_\mathrm{ln}(\mathbf{C}) - \mathcal{R}_\mathrm{nl}(\mathbf{f}_\mathrm{nl}) \tag{28}$$

with

$$\mathcal{R}_\mathrm{ln}(\mathbf{C}) = \int_0^T \langle \dot{\mathbf{x}}_\mathrm{c}(t+\tau), \mathbf{C}\dot{\mathbf{x}}_\mathrm{c}(t+\tau) \rangle \mathrm{d}\tau, \tag{29}$$

$$\mathcal{R}_\mathrm{nl}(\mathbf{f}_\mathrm{nl}) = \int_0^T \langle \dot{\mathbf{x}}_\mathrm{c}(t+\tau), \mathbf{f}_\mathrm{nl}(t+\tau) \rangle \mathrm{d}\tau \tag{30}$$

and

$$w^{1:1}(A, \mathbf{f}_\mathrm{ex}, t) = W^{1:1}(A, \mathbf{f}_\mathrm{ex}) \cos(\omega t - \alpha_{1,\mathrm{ex}}) \tag{31}$$

where $W^{1:1}(A, \mathbf{f}_\mathrm{ex}) = A\pi\sqrt{\langle \mathbf{a}_1^\mathrm{c}, \mathbf{f}_\mathrm{ex} \rangle^2 + \langle \mathbf{b}_1^\mathrm{c}, \mathbf{f}_\mathrm{ex} \rangle^2}$ and $\alpha_{1,\mathrm{ex}}$ is a phasing angle.

The Melnikov energy principle states that, for a given solution $\mathbf{x}_\mathrm{c}(t)$, if the amplitude of the work provided by the excitation forces $W^{1:1}$ is larger than the dissipation of both linear $\mathcal{R}_\mathrm{ln}$ and nonlinear $\mathcal{R}_\mathrm{nl}$ nonconservative effects, then the autonomous solution is associated with two periodic solutions in the actual perturbed system [19]. Three different cases are identified:

- $\left|W^{1:1}\right| > |\mathcal{R}_\mathrm{ln}| + |\mathcal{R}_\mathrm{nl}|$, two periodic solutions persist,
- $\left|W^{1:1}\right| = |\mathcal{R}_\mathrm{ln}| + |\mathcal{R}_\mathrm{nl}|$, a single periodic solution persists,
- $\left|W^{1:1}\right| < |\mathcal{R}_\mathrm{ln}| + |\mathcal{R}_\mathrm{nl}|$, no periodic solution persists.

The analysis of the sign of the function $\overline{\mathcal{M}} = \left|W^{1:1}\right| - |\mathcal{R}_{\text{ln}}| - |\mathcal{R}_{\text{nl}}|$ is sufficient to state on the existence of periodic solutions in the vicinity of autonomous conservative solutions [19].

In this paper, the methodology is based on the analysis of nonconservative autonomous solutions of complex nonlinear modes to estimate the Melnikov function, similarly to recent work carried out in the context of friction related nonlinearities [33]. For industrial models, damping effects can not be neglected in the computation of NNM justifying the use of nonconservative NNM. The slow exponential decay hypothesis made for the computation of complex nonlinear modes (see Sec. 2.4) reduces the influence of this choice on the accuracy of the method. Indeed, the dissipation associated with the damping ratio ζ is small over a single period. The use of damped NNM instead of conservative NNM is examined in the light of the results of Sec. 4.

2.6 Numerical isola detection procedure

The proposed numerical strategy for the research of isolated branches of solutions is composed of four steps:

1. a NFRC is computed for a given level of forcing and damping, see Fig. 3a,
2. the damped NNM of the system is computed, see Fig. 3b,
3. Melnikov's indicator is used to predict the location of solutions in forced response, see Fig. 3c,
4. new NFRC calculations are run in the area where isolated branches of solutions are predicted, see Fig. 3d.

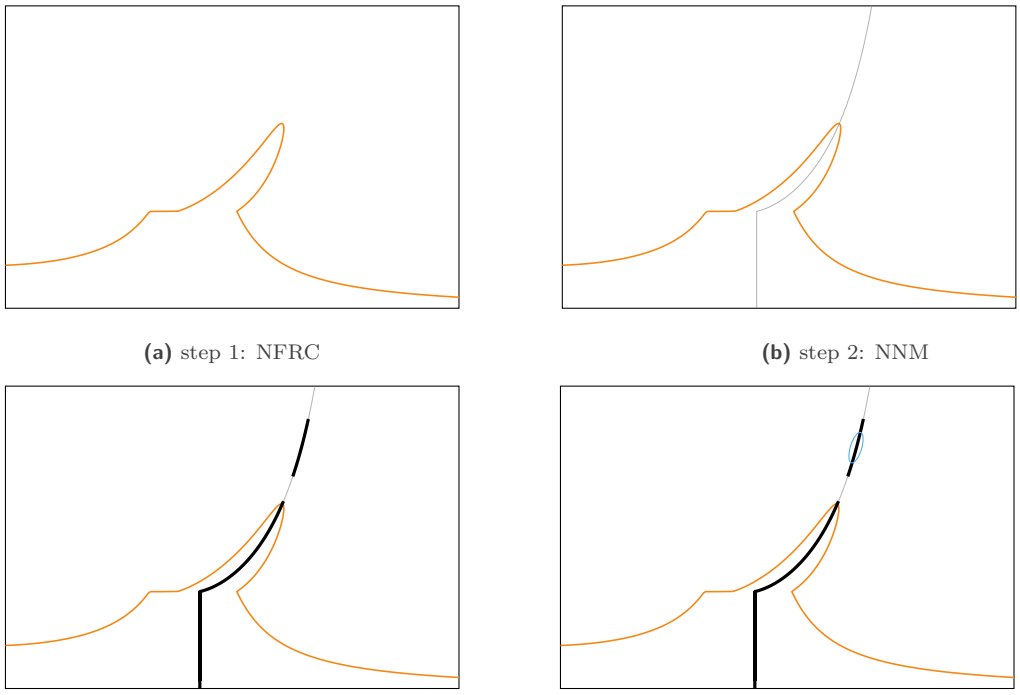

(a) step 1: NFRC

(b) step 2: NNM

(c) step 3: Melnikov analysis

(d) step 4: continuation

Figure 3. Numerical isola detection procedure, NFRC (—), NNM (—), Melnikov energy principle predicts persistence (—), isolated branch of solutions (—).

Figure 3 illustrates the proposed isola detection procedure, it also explains how isolated solutions are found in the vicinity of a NNM.

3 Blade tip/casing interaction on NASA rotor 67

3.1 Blade model

The industrial case study used in this work is the NASA rotor 67 fan blade [45], developed at NASA's Lewis research center as a benchmark blade for computational fluid dynamics codes [46]. More recently, it was used for the benchmark of numerical strategies accounting for blade-tip/casing interactions [16] where its intricate dynamics response was exhibited. The rotor is made out of a titanium alloy of grade 5: TA6V (Ti 6Al 4V). The material properties of this alloy are given in Tab. 1.

Young's modulus E	density ρ	Poisson coefficient ν
108 GPa	4,400 kg·m^{-3}	0.34

Table 1. Material properties retained for TA6V.

The full finite element mesh is composed of 129181 quadratic pentahedron elements adding up to 201287 nodes[1], see Fig. 4b. A reduced-order model is computed by using a Craig-Bampton procedure [47] where the root of the blade is assumed to be clamped. The reduced-order model is composed of $n_\mathrm{b} = 9$ boundary nodes evenly spaced along the blade tip and $\eta = 12$ internal modes. Modal damping is used with $\xi_{1-2} = 1 \cdot 10^{-3}$ for the first two bending modes (1B and 2B) and $\xi_{3+} = 5 \cdot 10^{-3}$ for the remaining modes. The eigenfrequencies of the first three modes are given in Tab. 2. The full NASA rotor 67 bladed disk is represented in Fig. 4a. In agreement with previous publications, only a single blade is considered in this study. In this paper, all the figures with NFRC are displayed for the radial displacement of the leading edge $r_1(t)$.

mode $\bullet$	1B	2B	1T	4	5
$\omega_\bullet$ (rad·s^{-1})	2,039.8	6,343.7	10,745.3	14,830.3	18,680.9
f (Hz)	324.6	1,009.6	1,710.2	2,973.2	2,973.2

Table 2. First eigenfrequencies of the blade.

(a) **(b)**

Figure 4. NASA rotor 67: full bladed disk [48] (a), finite element mesh (b).

[1] mesh available at https://lava-wiki.meca.polymtl.ca/public/modeles/rotor_67/

3.2 Contact scenario

Experimental findings highlighted that the vibration amplitudes of the casing are negligible in rubbing interactions. These observations allow to model the casing by a rigid mathematical profile. In this paper, a cylindrical casing is assumed, each boundary node is at a distance of $c_j = 4 \cdot 10^{-4}$ m for $j \in [\![1, n_\mathrm{b}]\!]$ at rest. Contact is initiated through the excitation of the whole blade along its first bending mode with a dimensionless amplitude A on the first harmonic, so that

$$\mathbf{f}_\mathrm{ex}(t) = A\mathbf{M}\mathbf{\Phi}_\mathrm{1B}\cos(\omega t). \tag{32}$$

Aforementioned key quantities are depicted in Fig. 5.

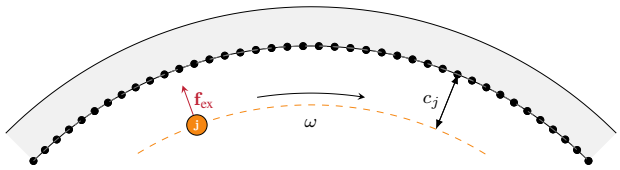

Figure 5. Circular casing (▭) in front of the j-th boundary node (●).

Given the high relative speeds involved in rubbing interactions, permanent sliding is assumed for the computation of dry friction forces. For the j-th boundary node at time t_i, it yields

$$f^\theta_{\mathrm{nl},j}(t_i) = \mu \frac{v^\theta_j(t_i) + \rho_j\omega}{\sqrt{(v^\theta_j(t_i) + \rho_j\omega)^2 + v^z_j(t_i)^2}} f^\mathrm{N}_{\mathrm{nl},j}(t_i) \tag{33}$$

and

$$f^z_{\mathrm{nl},j}(t_i) = \mu \frac{v^z_j(t_i)}{\sqrt{(v^\theta_j(t_i) + \rho_j\omega)^2 + v^z_j(t_i)^2}} f^\mathrm{N}_{\mathrm{nl},j}(t_i) \tag{34}$$

where $f^\theta_{\mathrm{nl},j}$ and $f^z_{\mathrm{nl},j}$ are the circumferential and axial friction forces, $\mu = 0.15$ is the dry friction coefficient, v^θ_j and v^z_j are the circumferential and axial velocities. ρ_j is the radial distance of the j-th boundary node from the rotation axis.

4 Numerical results

4.1 Isola detection procedure

A dynamic analysis of the investigated system is carried out with $A = 140$. The NNM of the system associated with the 1B mode is also computed as it is required for the Melnikov analysis. $N_\mathrm{h} = 10$ harmonics and $N_\mathrm{t} = 512$ instants are considered for the HBM computations and the DLFT-HBM parameter ε is set to $\varepsilon = 1 \cdot 10^7$ N·m^{-1}.

4.1.1 Melnikov energy principle

Both the work and dissipative terms of the Melnikov function $\overline{\mathcal{M}}^{1:1}$ are represented in Fig. 6: several wells of energy delimited by high amplitude peaks are observed for the dissipative term. The Melnikov energy principle states that if the work term (—) is greater than the dissipative term (also referred to as resistance) (—), then solutions persist in forced response. Accordingly, wells of energy are privileged areas for the existence of solutions in forced response. These areas translate into portions of the NNM—represented in black (—)—where the Melnikov energy principle states that solutions may exist in forced response, see Fig. 7. Conversely, areas of the NNM for which the dissipative term is greater than the work term are depicted using a lighter color (—). In total, six distinct portions of the NNM

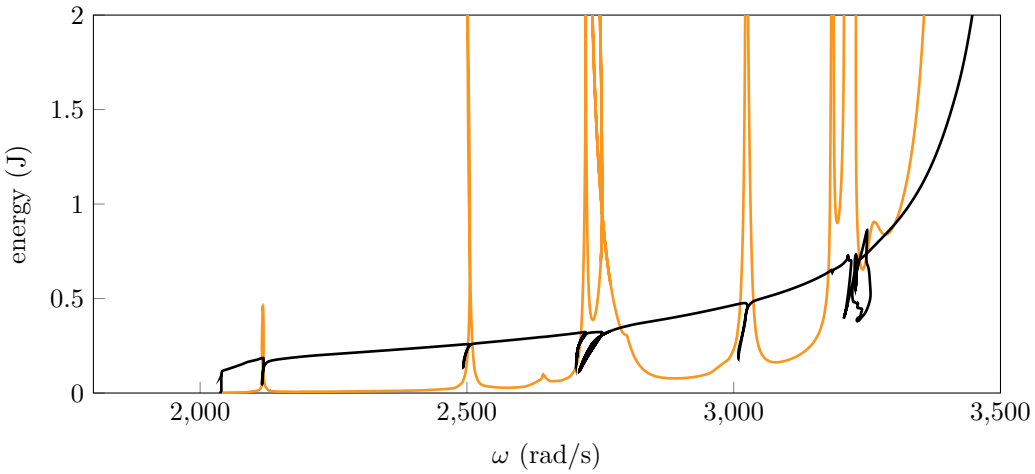

Figure 6. Energy principle for $A = 140$, dissipative term $|\mathcal{R}_{\text{ln}}| + |\mathcal{R}_{\text{nl}}|$ (—), work term $\left|W^{1:1}\right|$ (—).

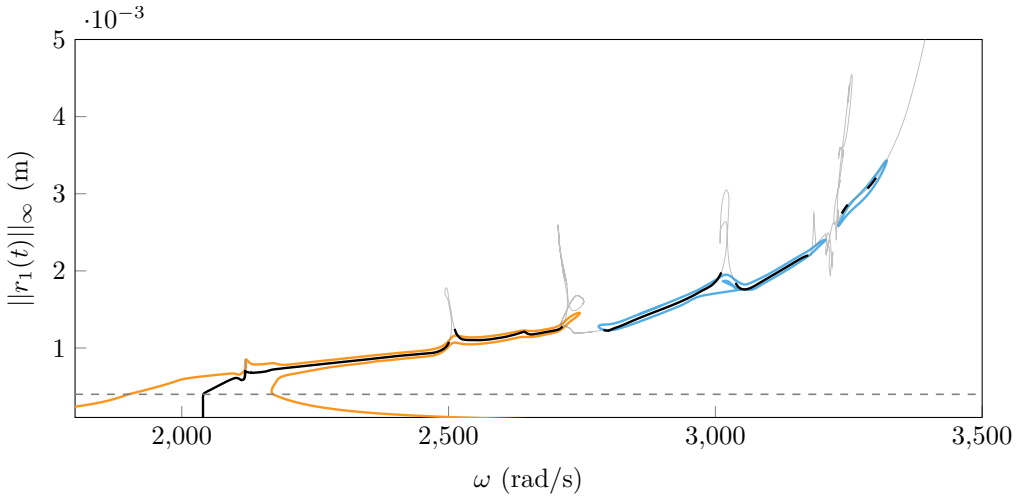

Figure 7. Application of the energy principle for $A = 140$, main NFRC (—), isolated branches of solutions (—), NNM ($\overline{\mathcal{M}}^{1:1} > 0$) (—), NNM ($\overline{\mathcal{M}}^{1:1} < 0$) (—), c_1 (- -).

for which solutions may exist are identified with the Melnikov energy principle. It is noticeable in Fig. 7 that the two first portions correspond almost perfectly to the main NFRC computed by DLFT-HBM (—). The four remaining portions however, correspond to much larger pulsations ($\omega \geq$ 2,750 rad·s^{-1}) and amplitudes ($\|r_1(t)\|_\infty \geq$ 1.5 mm). Carrying out DLFT-HBM computations using as initial guess the center of these areas yields the discovery of two distinct isolated branches of solutions (—) which underlines the relevance of the results obtained by application of the Melnikov energy principle. The isolated branch associated to the highest amplitudes corresponds to two small persistence areas and is not identified with the same level of precision as the other branch of isolated solutions. This slight defect is attributed to the fact that the resistance term displayed in Fig. 6 features small oscillations around $\omega = 3{,}250\,\text{rad}\cdot\text{s}^{-1}$ that cause $\overline{\mathcal{M}}^{1:1}$ to oscillate around zero.

Considering the small computational cost of the application of the Melnikov energy principle as well as the accuracy achieved on the predicted areas where solutions may exist, these first results underline the potential of the Melnikov energy principle for structural design purposes. The orders of magnitude of computational times associated

with the isola detection procedure on a computer equipped with a i7 CPU, say for the results of Fig. 7, is around 80 minutes (including the NNM, the Melnikov energy principle, the computation of the main NFRC and each isolated branch). For comparison purposes, the computational time of TI simulations—presented in Sec. 4.1.2—on the whole frequency range adds up to about 150 minutes (3 minutes per point), making it slower than the whole frequency domain strategy. Moreover, one can note that the computation of the NNM and the energy principle are carried out only once for all forcing amplitudes, making DLFT-HBM computations at other values of A even faster (around 30 minutes per level of forcing amplitude). In addition, it is important to emphasize that the DLFT-HBM based isola detection procedure also provides access to isolated branches that the TI is unable to account on its own.

Looking closely at the results, there remains small discrepancies between the Melnikov energy principle and DLFT-HBM simulations that are worth investigating. In particular, while the Melnikov energy principles yields six distinct portions of the NNM—which suggests that four isolated branches of solutions may exist beside of the main NFRC—only two isolated branches of solutions are found with DLFT-HBM. Interestingly, one may notice that portions of the NNM over which solutions are expected to be found are all separated by narrow areas of high amplitudes of the NNM, see Fig. 7. Peaks in the NNM—that translate into peaks of resistance in Fig. 6—cause the Melnikov energy principle to predict an interruption in solution persistence.

4.1.2 Numerical verification of DLFT-HBM solutions

In order to assess the physical relevance of the isolated branches of solutions detected in Fig. 7, TI simulations are run throughout the considered pulsation range. These simulations are carried out over a hundred periods using initial conditions taken from DLFT-HBM predicted solutions. Almost all TI simulations depicted in Fig. 8 reach

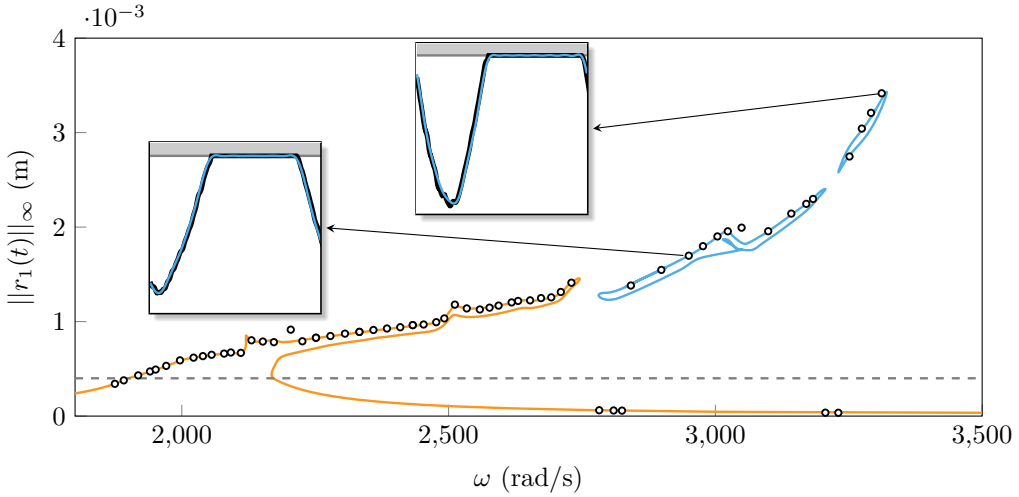

Figure 8. Correlation of TI and HBM simulations for $A = 140$, main NFRC (—), isolated branches (—), TI (○), c_1 (- -). Displacement graphs : DLFT-HBM (—), TI (—), casing (▭).

the same periodic orbits as the DLFT-HBM solutions. Contrarily to the DLFT-HBM, contact treatment in TI simulations is based on Lagrange multipliers [4]. Due to the distinct contact treatment algorithm and to the HBM implied harmonic truncation, the transfer of initial conditions from DLFT-HBM to TI is considered as a perturbation of the periodic solutions. For that reason, it is assumed that, if perturbed solutions reach the same periodic orbit after being integrated over many periods, these solutions are stable. From a design standpoint, because most of the solutions depicted in Fig. 8 are predicted to be stable, they could be of critical importance.

In addition, it is also shown in Fig. 8 that an excellent agreement is observed between TI and DLFT-HBM solutions in the time domain. This provides an *a posteriori* confirmation that the numerical parameters of the DLFT-HBM are properly chosen for the characterization of this nonlinear configuration. As pointed out in the literature [49], complex nonlinear normal modes may provide erroneous results in some cases. In this work, the fact

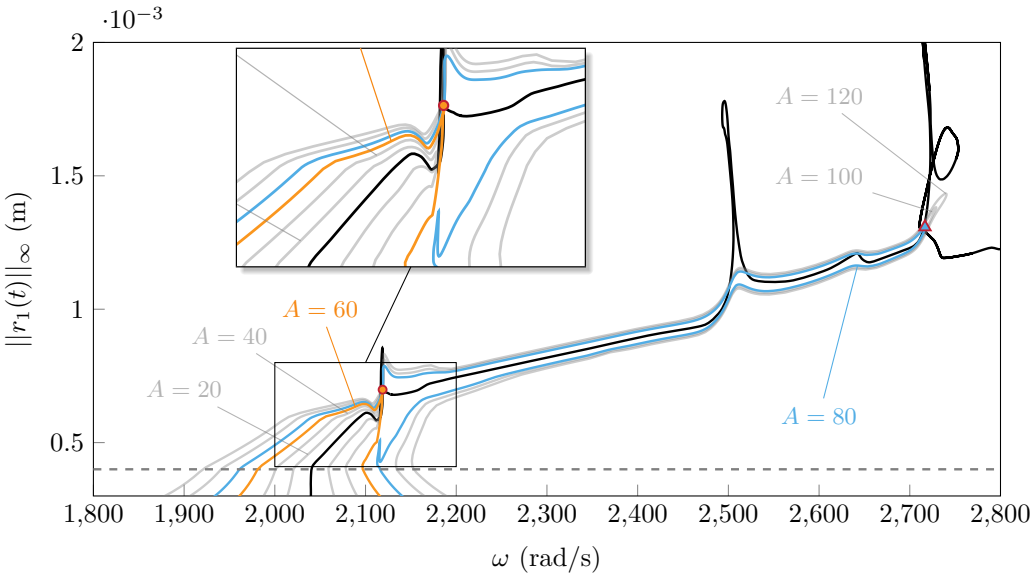

Figure 9. NFRC from $A = 20$ to $A = 120$, $A = 60$ (—), $A = 80$ (—), $A \in \{20, 40, 100, 120\}$ (—), NNM (—), c_1 (- -).

that DLFT-HBM and TI solutions are a perfect match in areas where the complex nonlinear normal mode predicted the existence of solutions provides an *a posteriori* proof that the use of complex nonlinear modes is reliable for this application.

4.2 Influence of the forcing amplitude

4.2.1 Nonlinear resonance frequency

In order to further analyze the dynamics of the blade, multiple forced responses are computed for various values of A from $A = 20$ to $A = 120$, see Fig. 9. The NNM of the system accurately describes the backbone curve of the system, to the exception of the narrow areas where peaks of amplitude are observed, as discussed in Sec. 4.1.1.

Looking at the NFRC obtained for each value of A, there is a very sudden increase of the predicted nonlinear resonance frequency between $A = 60$ (—) and $A = 80$ (—). Indeed, the computed NFRC for $A = 80$ features high amplitude solutions for pulsations as high as 2,700 rad·s^{-1} (▲), while the peak of amplitude for $A = 60$ is reached around 2,100 rad·s^{-1} (●). These preliminary results indicate that the value of the nonlinear resonance frequency predicted by DLFT-HBM is discontinuous with respect to A.

4.2.2 Isolated branches of solutions

The Melnikov energy principle is here applied for $A = 60$ and the results are depicted in Fig. 10. In addition to a portion of the NNM corresponding to the NFRC (—) plotted in Fig. 9, the Melnikov energy principle yields four additional areas—marked as 2, 3, 4 and 5 in Fig. 10—where solutions are expected. In a similar fashion to what was done in Sec. 4.1.1, solutions belonging to these areas are used to run DLFT-HBM simulations and three isolated branches of solutions (—) are found. The first isolated branch of solutions includes portions 2 and 3 of the NNM while the two other isolated branches respectively correspond to portions 4 and 5 of the NNM, see Fig. 10.

A better understanding of the previously witnessed discontinuity of the nonlinear resonance frequency predicted by DLFT-HBM with respect to A is thus obtained. Indeed, it seems that as A increases, the isolated branch of solution predicted for $A = 60$ around areas 2 and 3 becomes connected to the main NFRC. From a DLFT-HBM point of view, because a standard continuation algorithm is employed—and no isolated branch of solutions is computed—, this implies a sudden increase of the nonlinear resonance frequency. One may assume that similar phenomena are to be expected with the other isolated branches of solutions for much greater values of A.

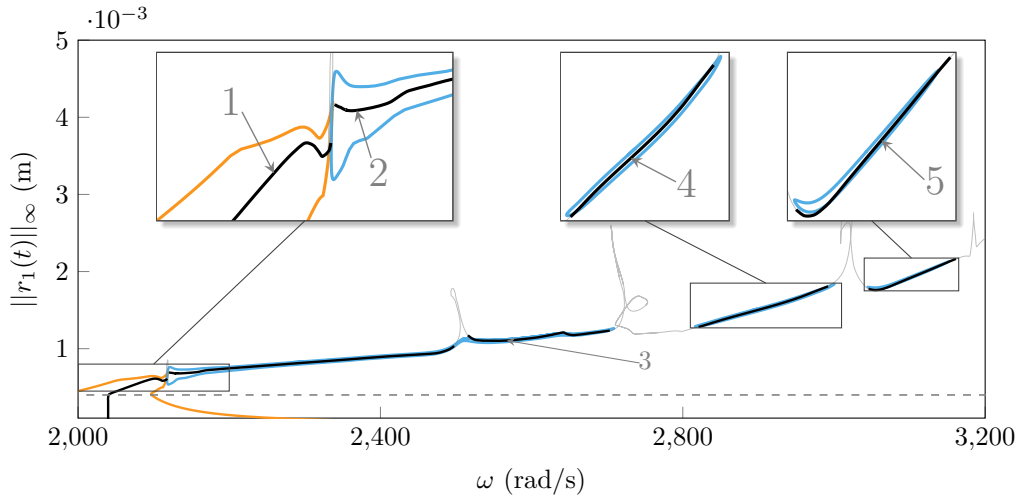

Figure 10. Application of the energy principle for $A = 60$, main NFRC (—), isolated branches of solutions (—), NNM ($\overline{\mathcal{M}}^{1:1} > 0$) (—), NNM ($\overline{\mathcal{M}}^{1:1} < 0$) (—), c_1 (- -).

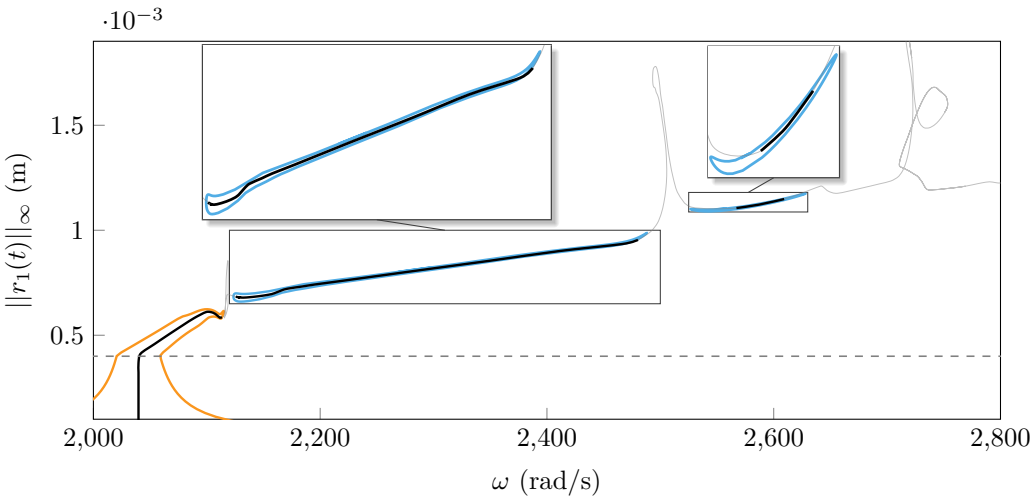

Figure 11. Application of the energy principle for $A = 20$, main NFRC (—), isolated branches of solutions (—), NNM ($\overline{\mathcal{M}}^{1:1} > 0$) (—), NNM ($\overline{\mathcal{M}}^{1:1} < 0$) (—), c_1 (- -).

In order to investigate the isolated branches at lower amplitudes, the value $A = 20$ is now studied. The application of the Melnikov energy principle to this configuration yields the results depicted in Fig. 11. Three portions are identified along the NNM for which solutions are expected in forced response. Same as above, in addition to the main NFRC (—) isolated branches of solutions (—) are found using the DLFT-HBM. For this lower value of A, it appears that the two isolated branches of solutions that are predicted emanate from a split of the first isolated branch of solutions predicted for $A = 60$. These observations indicate that branches of solutions may split in the vicinity of high amplitude areas on the NNM as A decreases.

At this point, the application of the Melnikov energy principle leads to the accurate prediction of areas where solutions exist for all levels of forcing amplitude. Moreover, it is possible to find solutions very remote from the DLFT-HBM predicted nonlinear resonance frequency. The use of a damped NNM, instead of a conservative one,

as proposed by Cenedese and Haller [19], still allows to accurately identify areas where solutions may exist. This observation allows to consider a wider variety of numerical strategies for the computation of autonomous families of solutions [33, 43, 44].

4.2.3 Evolution of the nonlinear resonance

In order to illustrate the assets of the proposed methodology, the stiffening phenomenon—the shift of the nonlinear resonance frequency due to contact interactions $\Delta\omega = \max(\omega) - \omega_{1B}$—and the maximum amplitude obtained for different values of A are depicted in Fig. 12. These quantities are obtained by three different approaches: the classical DLFT-HBM with arc-length continuation (●), the use of the Melnikov energy principle (●) and the combination of the Melnikov energy principle with the computation of isolated branches of solutions with DLFT-HBM (●). As

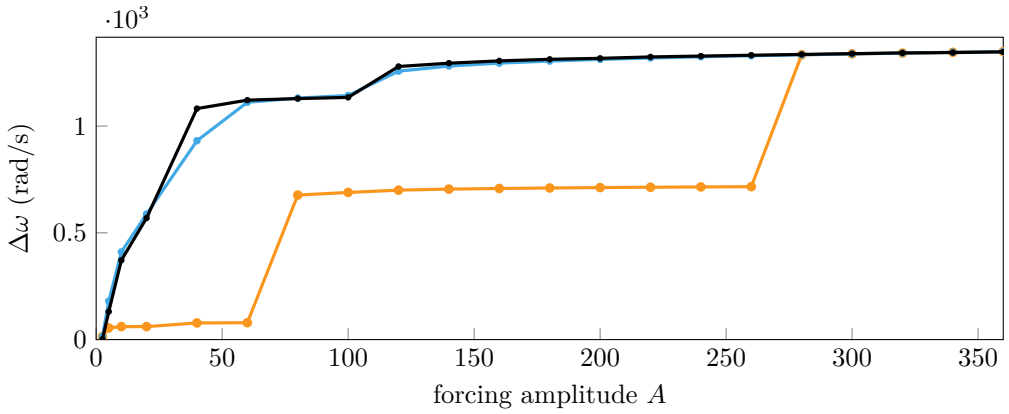

(a)

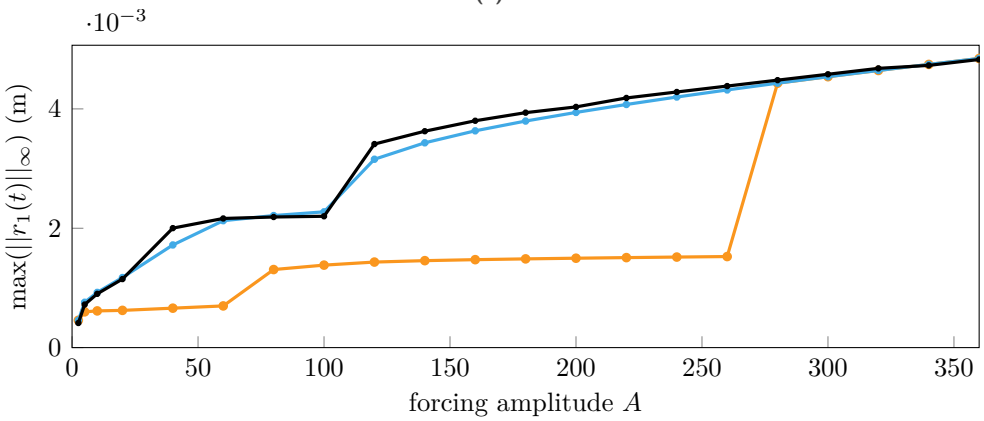

(b)

Figure 12. Evolution of the nonlinear resonance with respect to A, (a) stiffening effect, (b) maximum amplitude, main NFRC (●), energy principle alone (●), nonlinear resonance (with isolas) (●).

it can be seen in Fig. 12, this comparison underlines how the classical use of the DLFT-HBM with an arc-length continuation algorithm fails to accurately predict both the actual nonlinear resonance frequency and the maximum amplitude. The application of the Melnikov energy principle alone (●) allows to make a cheap, yet accurate, estimation of nonlinear resonance frequencies. A finer estimate may be obtained by computing associated isolated branches of solutions (●), but this comes at a significant computational cost.

4.3 Damping effects

The resistance term is directly related to the damping matrix $\mathbf{C}$. Because modal damping is here used to compute this matrix, individual modal damping ratios can numerically be adjusted at will so as to observe certain trends on the resistance curve. One may note that, since damped NNM are used in this work, the computation of a new NNM is required every time damping ratios are modified.

As an illustration, the influence of the modal damping of the fourth mode of eigenfrequency $\omega_4 = 14{,}830\,\mathrm{rad{\cdot}s^{-1}}$ is assessed. The result of this study is depicted in Fig. 13. By increasing the modal damping ratio of the fourth mode

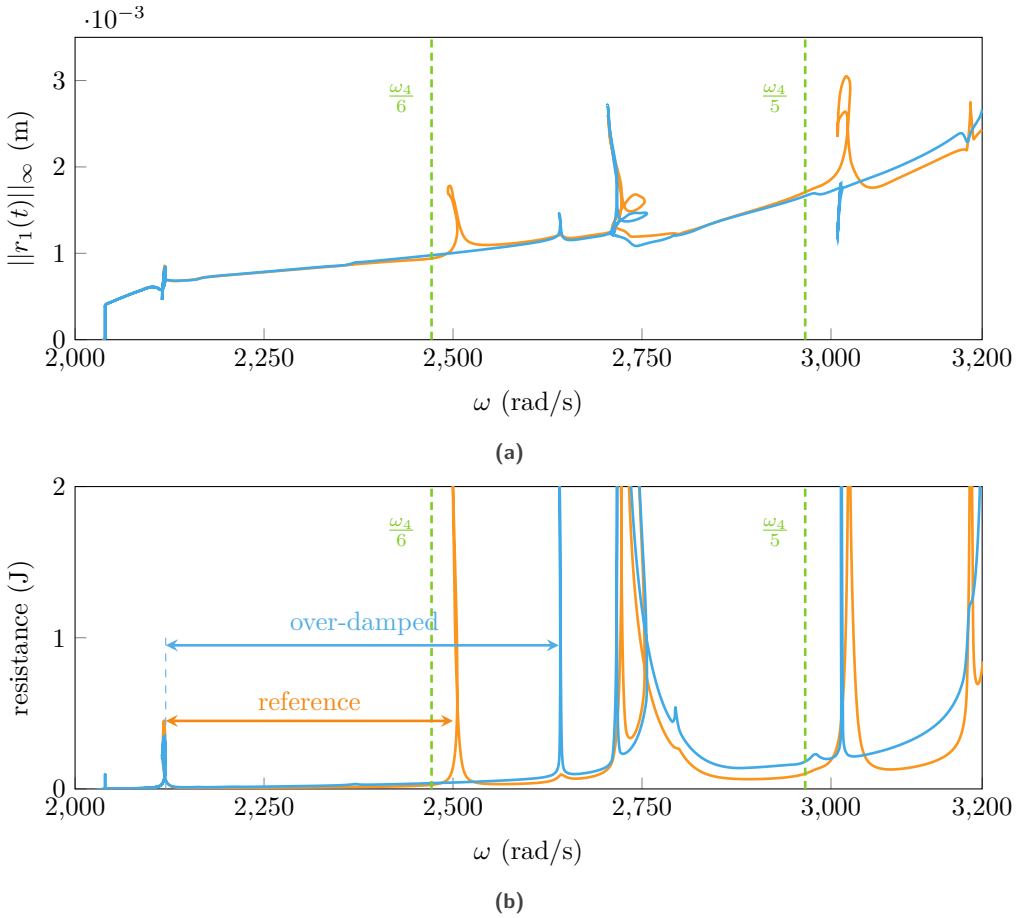

Figure 13. Impact of the value of the fourth mode modal damping ratio, (a) NNM, (b) resistance, $\xi_4 = 5 \cdot 10^{-3}$ (—), $\xi_4 = 0.5$ (—).

to $\xi_4 = 0.5$, the fourth mode is filtered away. In the mean time, two local peaks in the vicinity of $\omega = \frac{\omega_4}{5}$ and $\omega = \frac{\omega_4}{6}$ are attenuated on the NNM, as depicted in Fig. 13a. This supports the hypothesis that the peaks in the NNM are caused by nonlinear modal interactions as previously suggested in the literature [22, 24]. Moreover, the evolution of the resistance term is depicted in Fig. 13b where it is seen that the peaks in the resistance are also strongly attenuated so that the barriers of energy have almost vanished. Even though new—smaller and narrower—peaks appeared further on the curve, the well of energy associated with the barrier around $\omega = \frac{\omega_4}{6}$ has become wider, as represented in Fig. 13b. Without the proposed isola detection procedure, this observation could be considered as detrimental because the stiffening phenomenon is increased by filtering the fourth mode. However, by analyzing the resistance curve in Fig. 13b, one can see that the increase of ξ_4 only affects the connectivity of branches of solutions that would otherwise be isolated, thus not fundamentally impacting contact stiffening itself.

Additional investigations are conducted in order to explain why the two resistance peaks attributed to the fourth

mode remain even though the mode is filtered away. The relative modal contributions $||\gamma_j(t)||_{\infty,\text{rel}}$ of each mode along the NNM are examined. The relative modal contributions are computed following

$$\gamma_j(t_i) = \mathbf{\Phi}_j^\top \mathbf{M}\mathbf{x}(t_i) \quad \forall (i,j) \in [\![1, N_\text{t}]\!] \times [\![1, n]\!] \tag{35}$$

and

$$||\gamma_j(t)||_{\infty,\text{rel}} = \frac{\max\limits_{i\in[\![1,N_\text{t}]\!]} |\gamma_j(t_i)|}{\sum\limits_{k=1}^{n} \max\limits_{i\in[\![1,N_\text{t}]\!]} |\gamma_k(t_i)|}. \tag{36}$$

The 39 relative modal contributions of the NNM of Fig. 13 are depicted in Fig. 14 for both damping ratios.

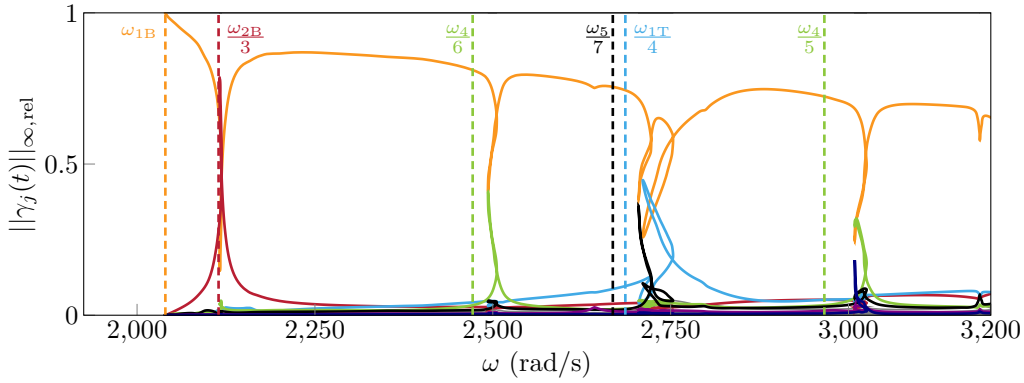

(a) $\xi_4 = 5 \cdot 10^{-3}$

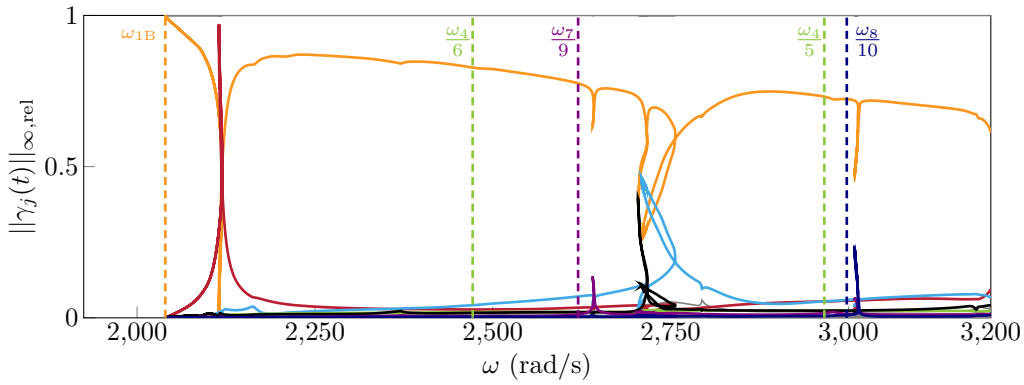

(b) $\xi_4 = 0.5$

Figure 14. Relative modal contributions, 1B mode (—), 2B mode (—), 1T mode (—), fourth mode (—), fifth mode (—), seventh mode (—), eighth mode (—), other modes (—).

Analyzing Fig. 14 yields that all peaks in the resistance curve in Fig. 13b and in the amplitude curve of the NNM in Fig. 13a can be attributed to a sudden decrease of the 1B mode contribution in Fig. 14. Each drop is also associated with an increase of the contribution of another mode. This phenomenon happens close to frequencies associated with fractions of the linear eigenfrequency of the mode that features a peak of contribution. Though, linear eigenfrequencies underestimate the frequencies of nonlinear modal interactions because all modes are stiffened due to contact interactions. By using a higher damping ratio for the fourth mode $\xi_4 = 0.5$, the drops in 1B modal contribution are annihilated around fractions of ω_4. However the seventh mode (—) and eighth

mode (—)—respectively associated with $\omega_7 = 23{,}579.1\,\mathrm{rad{\cdot}s^{-1}}$ and $\omega_8 = 29{,}975.8\,\mathrm{rad{\cdot}s^{-1}}$—now feature peaks of contributions, explaining why two peaks of resistance still exist in Fig. 13 after the fourth mode has been damped.

All these observations support the hypothesis that nonlinear modal interactions can be responsible for the separation of isolated branches of solutions from the main NFRC on this highly nonlinear application.

5 Conclusion

This paper demonstrates the applicability and accuracy of an isola detection procedure relying on the analysis of the damped NNM of a system featuring contact interfaces in the presence of harmonic forcing. The methodology is applied on the NASA rotor 67 industrial fan blade that constitutes a challenging case study for the characterization of rubbing interactions. A discontinuity of the nonlinear resonance frequency with respect to the amplitude of the applied harmonic forcing is evidenced. It is investigated in the light of the Melnikov energy principle and multiple isolated branches of solutions are captured. The isola detection procedure proves to be very accurate for multiple forcing levels when it comes to predict the existence of solutions in the vicinity of a NNM. It is shown that the use of typical continuation techniques alone underestimate both the response amplitude and the contact stiffening at the nonlinear resonance. Indeed, the use of the isola detection procedure allows to precisely locate the isolated nonlinear resonance without even computing the isolated branches yielding a large decrease in computational expense. A reference time marching strategy relying on Lagrange multipliers is used to demonstrate the stability of the periodic orbits belonging to isolated branches. The stability of these solutions could be assessed with the use of dedicated stability analyses, however the application of these strategies on industrial systems with contact interfaces is very recent [13], therefore exceeding the scope of this article. By using the proposed approach based on the Melnikov energy principle, new quantitative elements were highlighted in order to confirm the involvement of nonlinear modal interactions in the birth of isolated branches [22, 24].

Finally, this contribution opens up perspectives for the detection of isolated branches on systems featuring nonconservative and nonsmooth nonlinearities on high-dimensional industrial systems, such as friction damping applications [21].

Acknowledgments

This research was undertaken thanks to funding from the Canada Research Chairs Program.

References

[1] International Energy Agency. *Net Zero by 2050, a roadmap for the global energy sector*. 2021.

[2] A. Millecamps, J.-F. Brunel, P. Dufrénoy, F. Garcin, and M. Nucci. Influence of Thermal Effects During Blade-Casing Contact Experiments. *Proceedings of the ASME IDETC-CIE 2009*. 2009, pp. 855–862. DOI: 10.1115/DETC2009-86842. oai : hal-01223060.

[3] A. Millecamps, A. Batailly, M. Legrand, and F. Garcin. Snecma's Viewpoint on the Numerical and Experimental Simulation of Blade-Tip/Casing Unilateral Contacts. *Proceedings of the ASME Turbo Expo 2015*. 2015. DOI: 10.1115/GT2015-42682. oai : hal-01223582.

[4] N. J. Carpenter, R. L. Taylor, and M. G. Katona. Lagrange constraints for transient finite element surface contact. Int. J. Numer. Meth. Eng. Vol. 32, No. 1 (1991), 103–128. DOI: 10.1002/nme.1620320107. oai : hal-01389918.

[5] M. Legrand and C. Pierre. Numerical Investigation of Abradable Coating Wear Through Plastic Constitutive Law: Application to Aircraft Engines. *Proceedings of the ASME IDETC-CIE 2009*. 2009, pp. 907–916. DOI: 10.1115/DETC2009-87669. oai : hal-00413728.

[6] R. J. Williams. Simulation of Blade Casing Interaction Phenomena in Gas Turbines Resulting From Heavy Tip Rubs Using an Implicit Time Marching Method. *Proceedings of the ASME 2011 Turbo Expo*. 2011, pp. 1007–1016. DOI: 10.1115/GT2011-45495. oai : hal-01555287.

[7] S. K. Sinha. Rotordynamic analysis of asymmetric turbofan rotor due to fan blade-loss event with contact-impact rub loads. J. Sound Vib. Vol. 332, No. 9 (2013), 2253–2283. DOI: 10.1016/j.jsv.2012.11.033. oai : hal-01555281.

[8] S. Nacivet, C. Pierre, F. Thouverez, and L. Jezequel. A dynamic Lagrangian frequency–time method for the vibration of dry-friction-damped systems. J. Sound Vib. Vol. 265, No. 1 (2003), 201–219. DOI: 10.1016/S0022-460X(02)01447-5. oai : hal-01635272.

[9] L. Salles, B. Staples, N. Hoffmann, and C. Schwingshackl. Continuation techniques for analysis of whole aeroengine dynamics with imperfect bifurcations and isolated solutions. Nonlinear Dyn. Vol. 86, No. 3 (2016), 1897–1911. DOI: 10.1007/s11071-016-3003-y.

[10] E. P. Petrov. Multiharmonic Analysis of Nonlinear Whole Engine Dynamics With Bladed Disc-Casing Rubbing Contacts. *Proceedings of the ASME Turbo Expo 2012*. 2012, pp. 1181–1191. DOI: 10.1115/GT2012-68474.

[11] E. P. Petrov. Analysis of Bifurcations in Multiharmonic Analysis of Nonlinear Forced Vibrations of Gas Turbine Engine Structures With Friction and Gaps. J. Eng. Gas Turbines Power Vol. 138, No. 10 (2016), 12. DOI: 10.1115/1.4032906.

[12] L. Peletan, S. Baguet, M. Torkhani, and G. Jacquet-Richardet. Quasi-periodic harmonic balance method for rubbing self-induced vibrations in rotor–stator dynamics. Nonlinear Dyn. Vol. 78, No. 4 (2014), 2501–2515. DOI: 10.1007/s11071-014-1606-8. oai : hal-01061265.

[13] Y. Colaïtis and A. Batailly. Stability analysis of periodic solutions computed for blade-tip/casing contact problems. J. Sound Vib. Vol. 538 (2022), 117219. DOI: 10.1016/j.jsv.2022.117219. oai : hal-03764770.

[14] Y. Colaïtis and A. Batailly. Stability Analysis of an Industrial Blade Accounting for a Blade-Tip/Casing Nonlinear Interface. J. Eng. Gas Turbines Power Vol. 145, No. 4 (2022), 041003. DOI: 10.1115/1.4055492. oai : hal-03778471.

[15] E. P. Petrov. Stability Analysis of Multiharmonic Nonlinear Vibrations for Large Models of Gas Turbine Engine Structures With Friction and Gaps. J. Eng. Gas Turbines Power Vol. 139, No. 2 (2016). DOI: 10.1115/1.4034353.

[16] T. Vadcard, Y. Colaïtis, A. Batailly, and F. Thouverez. Assessment of Two Harmonic Balance Method-Based Numerical Strategies for Blade-Tip/Casing Interactions: Application to Nasa Rotor67. J. Eng. Gas Turbines Power Vol. 144, No. 12 (2022). DOI: 10.1115/1.4055416. oai : hal-03775621.

[17] T. Detroux, L. Renson, L. Masset, and G. Kerschen. The harmonic balance method for bifurcation analysis of large-scale nonlinear mechanical systems. Comput. Methods Appl. Mech. Eng. Vol. 296 (2015), 18–38. DOI: 10.1016/j.cma.2015.07.017. oai : hal-03446374.

[18] A. Grolet and F. Thouverez. Computing multiple periodic solutions of nonlinear vibration problems using the harmonic balance method and Groebner bases. Mech. Syst. Sig. Process. Vol. 52-53 (2015), 529–547. DOI: 10.1016/j.ymssp.2014.07.015. oai : hal-02121532.

[19] M. Cenedese and G. Haller. How do conservative backbone curves perturb into forced responses? A Melnikov function analysis. Proc. R. Soc. A. Vol. 476, No. 2234 (2020), 20190494. DOI: 10.1098/rspa.2019.0494.

[20] M. Volvert and G. Kerschen. Phase resonance nonlinear modes of mechanical systems. J. Sound Vib. Vol. 511 (2021), 116355. DOI: 10.1016/j.jsv.2021.116355.

[21] T. Heinze, L. Panning-von Scheidt, and J. Wallaschek. Global detection of detached periodic solution branches of friction-damped mechanical systems. Nonlinear Dyn. Vol. 99, No. 3 (2020), 1841–1870. DOI: 10.1007/s11071-019-05425-4.

[22] T. Detroux, J.-P. Noël, L. N. Virgin, and G. Kerschen. Experimental study of isolas in nonlinear systems featuring modal interactions. PLoS One Vol. 13, No. 3 (2018), 25. DOI: 10.1371/journal.pone.0194452.

[23] E. P. Petrov. A Method for Parametric Analysis of Stability Boundaries for Nonlinear Periodic Vibrations of Structures With Contact Interfaces. J. Eng. Gas Turbines Power Vol. 141, No. 3 (2019), 031023. DOI: 10.1115/1.4040850.

[24] F. Mangussi and D. H. Zanette. Internal resonance in a vibrating beam: a zoo of nonlinear resonance peaks. PloS one Vol. 11, No. 9 (2016), e0162365. DOI: 10.1371/journal.pone.0162365. oai : hal-01463863.

[25] R. Alcorta, S. Baguet, B. Prabel, P. Piteau, and G. Jacquet-Richardet. Period doubling bifurcation analysis and isolated sub-harmonic resonances in an oscillator with asymmetric clearances. Nonlinear Dyn. Vol. 98, No. 4 (2019), 2939–2960. DOI: 10.1007/s11071-019-05245-6. oai : hal-02295420.

[26] S. Benacchio, C. Giraud-Audine, and O. Thomas. Effect of dry friction on a parametric nonlinear oscillator. Nonlinear Dyn. Vol. 108, No. 2 (2022), 1005–1026. DOI: 10.1007/s11071-022-07233-9.

[27] G. Gobat, L. Guillot, A. Frangi, B. Cochelin, and C. Touzé. Backbone curves, Neimark-Sacker boundaries and appearance of quasi-periodicity in nonlinear oscillators: application to 1:2 internal resonance and frequency combs in MEMS. Meccanica Vol. 56, No. 8 (2021), 1937–1969. DOI: 10.1007/s11012-021-01351-1. oai : hal-03242876.

[28] A. Förster and M. Krack. An efficient method for approximating resonance curves of weakly-damped nonlinear mechanical systems. Comput. Struct. Vol. 169 (2016), 81–90. DOI: 10.1016/j.compstruc.2016.03.003.

[29] E. Sarrouy, A. Grolet, and F. Thouverez. Global and bifurcation analysis of a structure with cyclic symmetry. Int. J. Non Linear Mech. Vol. 46, No. 5 (2011), 727–737. DOI: 10.1016/j.ijnonlinmec.2011.02.005. oai : hal-00623630.

[30] C.-H. Lamarque and A. T. Savadkoohi. Algebraic techniques and perturbation methods to approach frequency response curves. Int. J. Non Linear Mech. Vol. 144 (2022), 104096. DOI: 10.1016/j.ijnonlinmec.2022.104096. oai : hal-03749838.

[31] T. L. Hill, A. Cammarano, S. A. Neild, and D. J. Wagg. Interpreting the forced responses of a two-degree-of-freedom nonlinear oscillator using backbone curves. J. Sound Vib. Vol. 349 (2015), 276–288. DOI: 10.1016/j.jsv.2015.03.030.

[32] J. Yuan, Y. Sun, C. Schwingshackl, and L. Salles. Computation of damped nonlinear normal modes for large scale nonlinear systems in a self-adaptive modal subspace. Mech. Syst. Sig. Process. Vol. 162 (2022), 108082. DOI: 10.1016/j.ymssp.2021.108082.

[33] Y. Sun, A. Vizzaccaro, J. Yuan, and L. Salles. An extended energy balance method arfor resonance prediction in forced response of systems with non-conservative nonlinearities using damped nonlinear normal mode. Nonlinear Dyn. Vol. 103 (2021), 3315–3333. DOI: 10.1007/s11071-020-05793-2.

[34] T. Vadcard, A. Batailly, and F. Thouverez. On Harmonic Balance Method-based Lagrangian contact formulations for vibro-impact problems. J. Sound Vib. Vol. 531 (2022), 116950. DOI: 10.1016/j.jsv.2022.116950. oai : hal-03665624.

[35] G. Von Groll and D. Ewins. The harmonic balance method with arc-length continuation in rotor/stator contact problems. J. Sound Vib. Vol. 241, No. 2 (2001), 223–233. DOI: 10.1006/jsvi.2000.3298. oai : hal-01333704.

[36] T. M. Cameron and J. H. Griffin. An Alternating Frequency/Time Domain Method for Calculating the Steady-State Response of Nonlinear Dynamic Systems. J. Appl. Mech. Vol. 56, No. 1 (1989), 149–154. DOI: 10.1115/1.3176036. oai : hal-01333697.

[37] D. Charleux, C. Gibert, F. Thouverez, and J. Dupeux. Numerical and Experimental Study of Friction Damping Blade Attachments of Rotating Bladed Disks. Int. J. Rotating Mach. Vol. 2006 (2006), 1–13. DOI: 10.1155/IJRM/2006/71302.

[38] L. Salles, A. M. Gouskov, L. Blanc, F. Thouverez, and P. Jean. Dynamic Analysis of Fretting-Wear in Joint Interface by a Multiscale Harmonic Balance Method Coupled With Explicit or Implicit Integration Schemes. *Proceedings of the ASME Turbo Expo 2010*. 2010, pp. 1003–1013. DOI: 10.1115/GT2010-23264. oai : hal-02529258.

[39] P. Wriggers and T. A. Laursen. Computational contact mechanics. 2006. DOI: \!10.1007/978-3-540-32609-0.

[40] L. Salles, L. Blanc, F. Thouverez, A. M. Gouskov, and P. Jean. Dynamic Analysis of a Bladed Disk With Friction and Fretting-Wear in Blade Attachments. *Proceedings of the ASME Turbo Expo 2009*. 2009, pp. 465–476. DOI: 10.1115/GT2009-60151.

[41] R. M. Rosenberg. Normal Modes of Nonlinear Dual-Mode Systems. J. Appl. Mech. Vol. 27, No. 2 (1960), 263–268. DOI: 10.1115/1.3643948.

[42] S. Shaw and C. Pierre. Non-linear normal modes and invariant manifolds. J. Sound Vib. Vol. 150, No. 1 (1991), 170–173. DOI: 10.1016/0022-460X(91)90412-D. oai : hal-01310674.

[43] M. Krack. Nonlinear modal analysis of nonconservative systems: Extension of the periodic motion concept. Comput. Struct. Vol. 154 (2015), 59–71. DOI: 10.1016/j.compstruc.2015.03.008.

[44] D. Laxalde and F. Thouverez. Complex non-linear modal analysis for mechanical systems: Application to turbomachinery bladings with friction interfaces. J. Sound Vib. Vol. 322, No. 4-5 (2009), 1009–1025. DOI: 10.1016/j.jsv.2008.11.044. oai : hal-00343494v3.

[45] D. C. Urasek and W. T. Gorrell. *Performance of two-stage fan having low-aspect-ratio first-stage rotor blading*. rapport technique. https://ntrs.nasa.gov/citations/19790018972. NASA Lewis Research Center Cleveland, OH, United States, 1979, p. 132.

[46] H. Doi and J. J. Alonso. Fluid/Structure Coupled Aeroelastic Computations for Transonic Flows in Turbomachinery. *Proceedings of the ASME Turbo Expo 2002*. 2002, pp. 787–794. DOI: 10.1115/GT2002-30313. oai : hal-01337402.

[47] R. R. Craig and M. C. C. Bampton. Coupling of substructures for dynamic analyses. AIAA J. Vol. 6, No. 7 (1968), 1313–1319. DOI: 10.2514/3.4741. oai : hal-01537654.

[48] D. Laity. *Stage 67 rotor and stage 67 casing half stators mounted. Records of the National Aeronautics and Space Administration, 1903 - 2006. Photographs relating to agency activities, facilities and personnel, 1973 - 2013*. https://catalog.archives.gov/id/17500553. 1980.

[49] M. Jahn, S. Tatzko, L. Panning-von Scheidt, and J. Wallaschek. Comparison of different harmonic balance based methodologies for computation of nonlinear modes of non-conservative mechanical systems. Mech. Syst. Sig. Process. Vol. 127 (2019), 159–171. DOI: 10.1016/j.ymssp.2019.03.005.